



## Article

# Analysis of the Fractal Dimension, *b*-value, Slip Ratio, and Decay Rate of Aftershock Seismicity Following the 6 February 2023 (Mw 7.8 and 7.5) Türkiye Earthquakes

Sherif M. Ali <sup>1,2,\*</sup> and Kamal Abdelrahman <sup>3,\*</sup>

<sup>1</sup> Preparatory Commission for the Comprehensive Nuclear-Test-Ban Treaty Organization (CTBTO), International Data Centre (IDC), 1400 Vienna, Austria

<sup>2</sup> National Research Institute of Astronomy and Geophysics (NRIAG), Helwan, Cairo 11421, Egypt

<sup>3</sup> Department of Geology and Geophysics, College of Science, King Saud University, P.O. Box 2455, Riyadh 11451, Saudi Arabia

\* Correspondence: sherif.ali@ctbto.org (S.M.A.); khassanein@ksu.edu.sa (K.A.)

**Abstract:** On 6 February 2023, Türkiye experienced a pair of consecutive earthquakes with magnitudes of Mw 7.8 and 7.5, and accompanied by an intense aftershock sequence. These seismic events were particularly impactful on the segments of the East Anatolian Fault Zone (EAFZ), causing extensive damage to both human life and urban centers in Türkiye and Syria. This study explores the analysis of a dataset spanning almost one year following the Türkiye mainshocks, including 471 events with a magnitude of completeness ( $M_c$ )  $\geq 4.4$ . We employed the maximum likelihood approach to estimate the *b*-value and Omori-Utsu parameters ( $K$ ,  $c$ , and  $p$ -values). The estimated *b*-value is  $1.21 \pm 0.1$ , indicating that the mainshocks occurred in a region characterized by elevated stress levels, leading to a sequence of aftershocks of larger magnitudes due to notable irregularities in the rupture zone. The aftershock decay rate ( $p$ -value =  $1.1 \pm 0.04$ ) indicates a rapid decrease in stress levels following the main shocks. However, the  $c$ -value of  $0.204 \pm 0.058$  would indicate a relatively moderate or low initial productivity of aftershocks. Furthermore, the  $k$ -value of  $76.75 \pm 8.84$  suggests that the decay of aftershock activity commenced within a range of approximately 68 to 86 days following the mainshocks. The fractal dimension ( $D_c$ ) was assessed using the correlation integral method, yielding a value of  $0.99 \pm 0.03$ . This implies a tendency toward clustering in the aftershock seismicity and a linear configuration of the epicenters. The slip ratio during the aftershock activity was determined to be 0.75, signifying that 75% of the total slip occurred in the primary rupture, with the remaining fraction distributed among secondary faults. The methodologies and insights acquired in this research can be extended to assist in forecasting aftershock occurrences for future earthquakes, thus offering crucial data for future risk assessment.



**Citation:** Ali, S.M.; Abdelrahman, K. Analysis of the Fractal Dimension, *b*-value, Slip Ratio, and Decay Rate of Aftershock Seismicity Following the 6 February 2023 (Mw 7.8 and 7.5) Türkiye Earthquakes. *Fractal Fract.* **2024**, *8*, 252. <https://doi.org/10.3390/fractalfract8050252>

Academic Editors: Mei Yin, Mengxi Zhang, Yi Rui, Zine El Abiddine Fellah and Carlo Cattani

Received: 20 February 2024

Revised: 8 April 2024

Accepted: 23 April 2024

Published: 25 April 2024



**Copyright:** © 2024 by the authors. Licensee MDPI, Basel, Switzerland. This article is an open access article distributed under the terms and conditions of the Creative Commons Attribution (CC BY) license (<https://creativecommons.org/licenses/by/4.0/>).

**Keywords:** fractal dimension; *b*-value; decay rate; slip ratio; Omori–Utsu; Türkiye

## 1. Introduction

Türkiye is located in the Alpine–Himalayan mountain belt, which is known for its high level of tectonic activity. It lies on the boundaries of the Eurasian, African, and Arabian plates, making it one of the most geologically dynamic regions in the world [1]. This region is characterized by active earthquake fault zones, including the North Anatolian Fault (NAF), East Anatolian Fault (EAF), and West Anatolian Fault (WAF) zones. These fault zones have the potential to generate destructive earthquakes, as evidenced by past events such as the 1999 Mw 7.6 Izmit, 1999 Mw 7.2 Düzce, 2011 Mw 7.1 Van, 2020 Mw 6.8 Elazığ, and 2020 Mw 7.0 Izmir earthquakes. The movement of the Arabian, Eurasian, and African plates, along with the Anatolian tectonic block, is primarily responsible for the significant seismic activity in Türkiye. The geological evolution of the area is a result of various significant interactions between major plate boundaries. These interactions

involve subduction, extensive transform faulting, the formation of mountains through compression, and the extension of the Earth's crust. The convergence of the African and Arabian plates with the Eurasian plate led to the closure of the Mediterranean Sea, resulting in the westward movement of the Anatolian block. This movement is predominantly accommodated along the North and East Anatolian faults. The convergence (subduction) boundary between the African plate in the south and the Anatolian block in the north is represented by the Cyprus Arc.

In 1999, Türkiye experienced one of its most catastrophic earthquakes in recent history, measuring 7.6 in magnitude near Izmit. This tragic event resulted in the loss of more than 16,900 lives and left a vast number of individuals without homes [2]. However, the impact of the disaster reached new levels on 6 February 2023, when a seismic event of significant magnitude, measuring 7.7, struck near Pazarcik city in southern Turkey. This was followed by a second earthquake, measuring 7.5 magnitude, near Elbistan city 9 h later. The focal depths of these earthquakes were recorded at 8.6 km and 7.0 km, respectively. Fourteen days later, another significant earthquake with a magnitude of 6.4 occurred in Define, Hatay. The aftermath of these earthquakes was marked by over 11,000 aftershocks, as reported by Türkiye's Disaster and Emergency Management Authority (AFAD). In total, more than 50,000 lives were lost, over 107,000 injuries were sustained, and extensive damage occurred across multiple provinces.

When such an event occurs, it is commonly assumed that neighboring regions experience an increase in stress. Over time, these stresses are relieved, resulting in aftershocks [3–9]. The current study aims to provide detailed and precise statistical inferences regarding the sequence of aftershocks in Kahramanmaraş. To achieve this, the statistical evolution of the aftershock data was analyzed, including parameters such as the *b-value*, decay rate (*p-value*), fractal dimension (*Dc-value*), and slip ratio. These analyses shed light on the seismotectonic properties of the area. Additionally, the changes in Coulomb stress resulting from the mainshock coseismic slip were evaluated to explain the occurrence of aftershocks. This study focuses on examining the geographic distribution of the Kahramanmaraş sequence and sheds light on the underlying faults responsible for it. By analyzing this sequence, we can gain valuable knowledge about the local tectonic activity. It is crucial to uncover the geometry of the fault zone in order to comprehend the evolution of faults and the mechanics behind earthquake rupture. The findings of this research will contribute to the development of a comprehensive earthquake hazard model for the region.

Several studies, including [10–12], have utilized global earthquake catalogs to gain insights into the complexity of earthquakes and to make predictions about their occurrence in terms of size, time, and location. Additionally, these studies have employed two robust empirical laws, namely the Gutenberg–Richter law and the Omori law, to characterize seismicity patterns. It has been observed that the productivity of aftershocks and the rate at which they decay are influenced by the faulting style of the mainshock. Specifically, strike-slip events exhibit a lower aftershock rate and a larger *p-value* compared to thrust and normal events, respectively [11]. In the studied region and its surroundings, the sinistral strike-slip mechanism of the East Anatolian Fault Zone (EAFZ) and Dead Sea Fault Zone (DSFZ)—along with the Cyprus Arc (CA) in southern Turkey, and the dextral strike-slip dominance along the North Anatolian Fault Zone (NAFZ) in the north—primarily accommodate the motion. This dynamic could potentially lead to an increased decay rate and a decrease in aftershock productivity [13].

## 2. Tectonic Summary and Seismicity

### 2.1. Tectonics and Historical Seismicity of the Anatolian Block

The Anatolian block is enclosed by the North Anatolian Fault Zone (NAFZ) in the north and the East Anatolian Fault Zone (EAFZ) in the southeast (Figure 1). Within this area, the NAFZ—which is a right-lateral strike-slip fault trending in an east–west direction—intersects with the EAFZ; a left-lateral strike-slip fault trending in a northeast–southwest direction. This interaction leads to a compression of the continent towards the east and an extension regime

towards the west. The movement between the Arabian plate and Eurasia results in the lateral escape of the northeast Anatolian block towards the east and the Anatolian block towards the west [14]. The Anatolian block exhibits a westward movement at a rate of approximately 25 mm/year in relation to Eurasia [14]. The primary mechanism accommodating this motion is the right-lateral strike-slip NAF located in northern Türkiye. Over the period spanning from 1939 to 1999, a sequence of highly destructive strike-slip earthquakes with a magnitude ( $M_w$ ) of 7.0 or greater propagated westward along the NAF system [15,16]. The farthest westward occurrence among these seismic events was the  $M_w$  7.6 Izmit (Kocaeli) earthquake of 17 August 1999. This devastating earthquake, which occurred near the Sea of Marmara, resulted in an approximate loss of 17,000 lives.

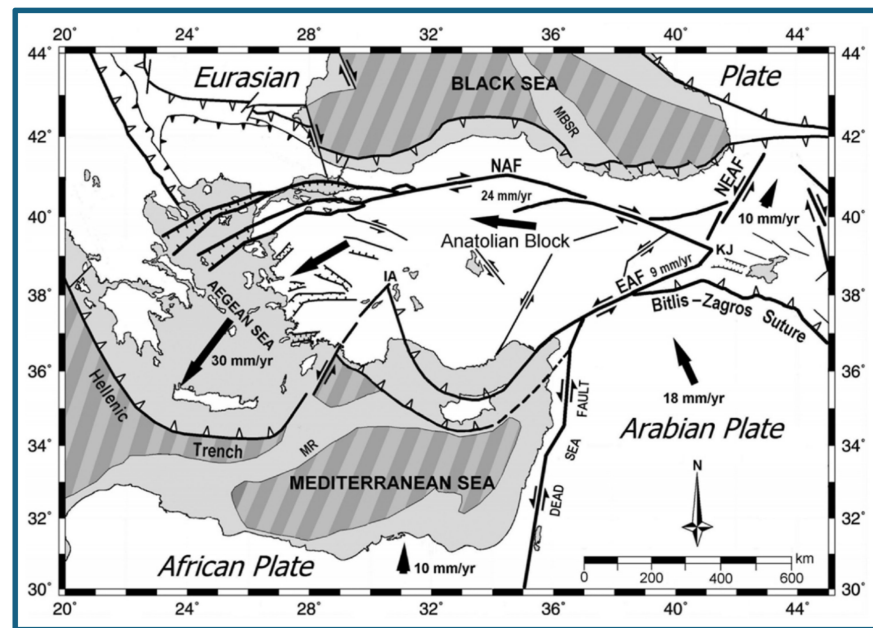


**Figure 1.** Map displaying the primary tectonic formations surrounding the Anatolian plate on a base taken from Nasa's World Wind software snapshots. The displacement vectors of the Arabian and Anatolian Plates relative to the Eurasian Plate are shown by the arrows. The locations of the different structures have been taken from various published maps. The major tectonic entities showing the fault and fold systems in the studied region are presented [12].

The Anatolian block, which is located in the southeastern region, exhibits a south-westward movement of approximately 15 mm/year in relation to the Arabian plate [14]. This lateral strike-slip motion is primarily observed along the EAF. Although no significant earthquakes with a magnitude of 7.0 or higher have occurred on this fault prior to 2023 in the last century, it remains seismically active. Notably, on 24 January 2020, a devastating  $M_w$  6.7 earthquake occurred, resulting in the loss of more than 40 lives (Figure 2). Moving further south, the Dead Sea fault, which runs in a northward direction, serves as a system of strike-slip mechanisms that enables varying movement between the African plate and the Arabian plate. The Arabian plate (situated at the southern extremity of the Dead Sea fault) steadily advances northward to the African plate at a rate of approximately 10 mm/year, gradually decreasing as one moves towards the north [17]. Historically, a significant earthquake along the Dead Sea fault occurred in November 1759, which struck near the Beqaa Valley of Lebanon and is estimated to have caused the loss of the lives of between 2000 and 20,000 individuals. In southern Türkiye, a complex deformation zone is formed and the transition area between the Dead Sea fault and the EAF experienced two major earthquakes in 2023, measuring  $M_w$  7.8 and  $M_w$  7.5. This earthquake sequence resulted in significant ruptures along the southwestern third of the EAF and the northernmost section of the Dead Sea fault [11–17].

## 2.2. Seismicity: 1900–2022

Türkiye has experienced a total of 21 earthquakes with a magnitude of 7.0 or higher since 1900. Of these, 11 took place either directly on or in close proximity to the North Anatolian Fault, five were located in western Türkiye's extensional region, three were situated in the eastern-most part of Türkiye, and the remaining two earthquakes occurred in 2023 with magnitudes of 7.8 and 7.5, on the most southern part of the EAF. The most significant earthquake recorded on the EAF was the 1905 (Mw 6.8) earthquake, which took place within the fault system's central region. The most devastating earthquakes in Türkiye since the beginning of the 20th century were the 1939 Erzincan earthquake with a magnitude of 7.8; this resulted in the death of over 32,000 people and injured more than 100,000; and the 1999 Izmit (Kocaeli) earthquake with a magnitude of 7.6, which claimed the lives of over 17,000 individuals and injured more than 50,000 [15–21].

Throughout the 20th century, a significant portion of the NAF experienced a series of powerful earthquakes, measuring at least Mw 7.0, that occurred in an east to west direction. Simultaneously, the EAF witnessed numerous Mw 6.0 earthquakes, primarily concentrated in its northernmost section. However, starting from the Mw 6.7 earthquake sequence in 2020, followed by the recent Mw 7.7 and M 7.5 earthquake sequences in 2023. The Mw 6.7 earthquake on 24 January 2020 took place either on or near the EAF (Figure 2) [21]. The faulting mechanism and the distribution of aftershocks associated with this earthquake indicate that the faulting occurred on a near vertical plane with a southwest–northeast orientation. The displacement on this plane aligns with the orientation of regional faults and the local plate motions [15,21].

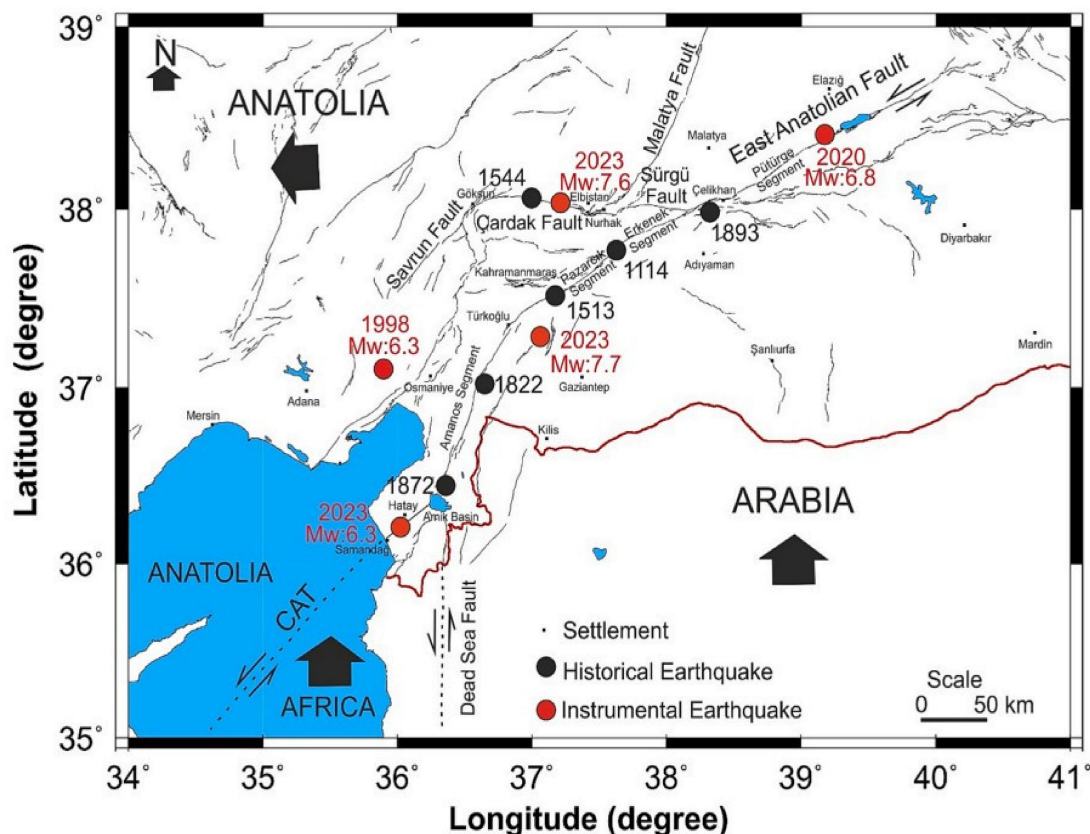


**Figure 2.** A map illustrating the destructive earthquakes that have taken place in the area, spanning both historical and instrumental eras. The diagram was produced using The Generic Mapping Tools (GMT) (after [21]).

### 2.3. 6 February 2023, Türkiye Earthquakes

On 6 February 2023, two devastating earthquakes took place in Kahramanmaraş, Türkiye. These two earthquakes had epicenters that were in very close proximity to each other. The initial earthquake occurred at 01:17 (GMT), reaching a depth of approximately 8.5 km. Subsequently, at 10:24 (GMT), the second earthquake ensued, registering a depth of about 7.0 km (Figure 3). According to the Kandilli Observatory and Earthquake Research Institute (KOERI), the magnitude of the first earthquake was estimated to be  $M_w$  7.7, while the Incorporated Research Institutions for Seismology (IRIS) and the U.S. Geological Survey (USGS) estimated it to be  $M_w$  7.8. This earthquake was the most powerful on record since the 1939  $M_w$  7.8 Erzincan earthquake. The second earthquake, which took place about 90 km north of the mainshock, had a magnitude determined as  $M_w$  7.6 by KOERI and  $M_w$  7.5 by both the IRIS and USGS (Figure 3).

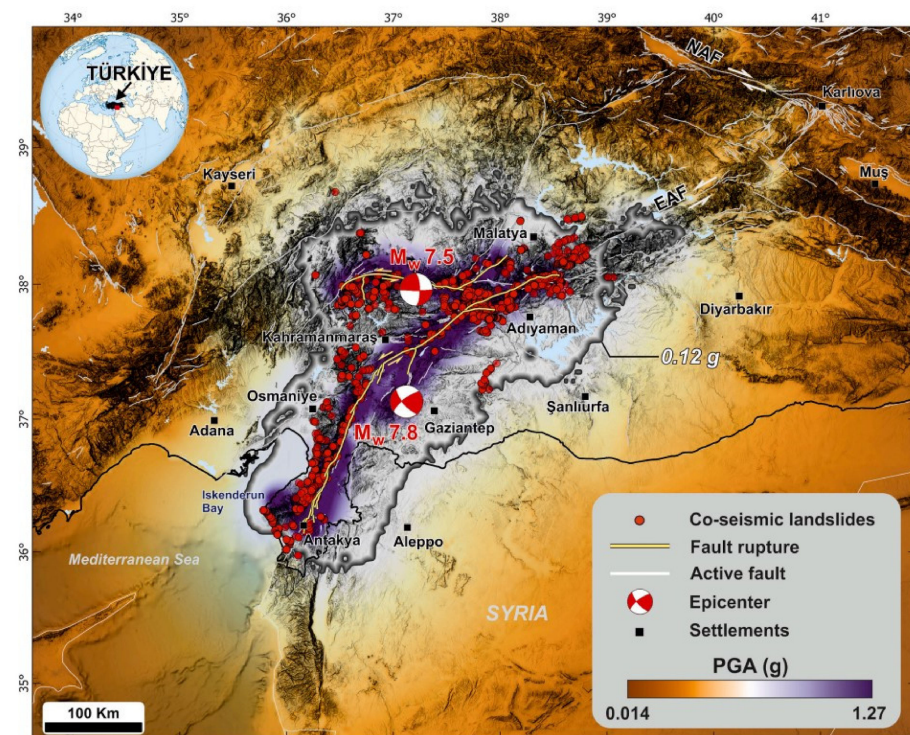


**Figure 3.** The spatial distribution of coseismic landslides triggered by the two main earthquake epicenters [22,23] fault rupture (yellow, [24]) and the USGS composite peak ground acceleration (PGA) map representing the maximum PGA recorded at each location for all earthquakes of magnitude 5.5 and larger from the sequence [25]. Major active faults [26] are indicated by white lines. EAF: Eastern Anatolian Fault, NAF: North Anatolian Fault. The 0.12 g PGA contour is shown with a dark grey line (For interpretation of the references to color in this figure legend, the reader is referred to the web version of this article) (After Görüm et al. [13]).

The shallow depth strike-slip faulting caused a magnitude 7.8 earthquake. This seismic event occurred either on a fault line that is either nearly vertical and left-lateral, with a NE–SW orientation; or right-lateral, with a SE–NW orientation. The earthquake’s epicenter suggests that it occurred close to a triple-junction involving the Anatolia, Arabia, and Africa tectonic plates. The earthquake’s mechanism and location align with it happening on either the EAFZ or the Dead Sea transform fault zone. The region where the earthquake sequence of  $M_w$  7.5 occurred on 6 February 2023 is seismically active, although the seismicity is moderate ( $<M_w$  7) compared to the nearby plate boundary zones in Türkiye. The epicenter of this event is situated on the Sürgü fault, directly west of the EAF [13].

### 3. Data Collection, Methodology, and Data Analyses

The Incorporated Research Institutions for Seismology (IRIS) is a non-profit consortium consisting of more than 120 universities in the United States. Its primary focus is on the acquisition, management, and distribution of seismological data, while also fostering collaboration among researchers globally. IRIS is committed to advancing our understanding of the Earth through seismological research, education, and outreach. The organization strongly advocates for open access to seismic data and tools, ensuring that the global scientific community can benefit from them. IRIS operates multiple data centers that gather, store, and disseminate seismic data from various networks across the globe. These data centers offer real-time and historical seismic data, as well as analysis and visualization tools. With a network of over 150 stations, IRIS offers a comprehensive global span for studying seismic activities and structure of the Earth's interior.

The earthquake data within a specified region, defined by latitudes  $35.0^{\circ}$ – $39.0^{\circ}$  N and longitudes  $34.0^{\circ}$ – $41.0^{\circ}$  E, has been compiled for the period between 6 February 2023 and 10 January 2024. This dataset consists of 471 local earthquakes, ranging in magnitude from 3.3 to 7.8, and focal depths vary between 0 to 27 km. To quantitatively analyze these data and the subsequent aftershock sequence, we have utilized two widely recognized scaling relationships in our study: the Gutenberg–Richter (G-R) frequency magnitude law [27] and the Modified Omori's Law /Omori–Utsu relationship [28]. Statistical analyses of the dataset have been conducted using the ZMAP (version 6.0) software package [29], a commercial software language which incorporates a range of tools written in Matlab<sup>®</sup>. The software package comes with a graphical user interface (GUI), which offers various features such as catalog quality assessment (including artifact detection, and completeness evaluation), exploratory data analysis, identification of seismicity, and fractal dimension determination.

#### 3.1. *b*-values and Magnitude of Completeness ( $M_c$ )

The earthquake frequency–magnitude distribution (FMD), commonly referred to as the Gutenberg–Richter relationship, is a commonly used power-law relation in seismicity studies. It was first introduced by [30] and further developed by [27]. This relationship establishes a correlation that links the frequency of earthquake occurrences with the distribution of magnitudes. This relationship is defined by Equation (1), which relates the cumulative seismic event count,  $N(M)$ , with magnitudes  $M$  and higher.

$$\log_{10}N(M)=a-b M \quad (1)$$

The seismicity parameters constants, denoted as ' $a$ ' and ' $b$ ', play a crucial role in seismology. The parameter ' $a$ ' represents the level of seismicity, while ' $b$ ' signifies the slope of the FMD. In particular, the parameter ' $b$ ' holds great importance in seismology due to its association with various geotectonic characteristics of a specific region [31,32]. Over the past several years, seismologists have extensively utilized the significance of ' $b$ ' in earthquake prediction [33,34] and for quantifying seismicity [35]. The *b*-value has been found to vary significantly on a local scale, ranging from 0.3 to 2.5 [36–42]. These variations can be attributed to various factors such as tectonic setting, focal depth, crustal heterogeneity, incomplete catalog data, predominant stress state, clustering of events, geothermal gradient, pore pressure, environmental or geophysical specifications, and method of calculation. All these elements, except for the method of calculation, are connected to the state of stress, either explicitly or implicitly [43]. However, in most cases, the *b*-value remains near one for extended durations and vast regions. In addition to indicating earthquake distribution, the *b*-value also provides insights into the stress conditions of a region [44].

It seems that an increase in the *b*-value above 1.0 suggests regions with minimal exerted stress and crustal diversity, whereas values below 1.0 indicate significant unequal stress and uniformity of crust composition [45–47]. Nevertheless, there are multiple approaches employed to compute the *b*-value. In this study, we evaluated the *b*-value using the Maximum Likelihood (ML) approach, which is implied in Equation (1). It is the most robust and

widely acknowledged technique for calculating the *b-value*, as proposed by Aki [48] using the following formula:

$$b = \frac{1}{\log_{10} \left[ \bar{M} - (M_{min}) - \frac{\Delta M}{2} \right]} \quad (2)$$

where the minimum magnitude  $M_{min}$  represents the magnitude of completeness ( $M_c$ ) or the threshold magnitude for earthquakes, while the mean magnitude  $\bar{M}$  and magnitude resolution  $\Delta M$  are also important factors. The  $M_c$  plays a crucial role in seismicity research, serving as the minimum magnitude required for accurate reporting of earthquake magnitudes. Determining  $M_c$  can be achieved by assuming the power-law distribution of G-R in relation to magnitude, as suggested by Wiemer and Wyss [46].

The Frequency Magnitude Distribution (FMD) chart provides a visual representation of various aspects of the data and their analysis. In the FMD chart, a straight line is typically used to represent the best-fit line according to the Gutenberg–Richter frequency–magnitude relationship. Squares on the chart represent the actual observed data points for specific magnitude intervals, while triangles are often used to denote estimated cumulative frequencies or other derived data points. The slope of the straight line (the *b-value*) is critical for understanding the seismic characteristics of the region. A steeper slope indicates a higher frequency of smaller earthquakes relative to larger ones. Each square corresponds to a magnitude range and shows the number of earthquakes that occurred within that range during the observation period. The use of triangles to represent estimated cumulative frequencies allows researchers to visually assess the fit of the Gutenberg–Richter model across the entire magnitude range, especially in cases where data may be sparse or incomplete. This helps in identifying any discrepancies between observed data (squares) and model expectations (straight line). The distribution of the squares and triangles on the chart can also help in assessing the completeness of the seismic catalog and identifying any potential anomalies in the observed seismicity. Deviations from the straight line—such as a flattening of the curve at low magnitudes, indicated by the distribution of triangles and squares, may suggest issues with the magnitude of completeness ( $M_c$ ) or a change in seismicity pattern, such as seismic quiescence or swarm-like behavior [43–46].

### 3.2. Decay Rate of Aftershocks (*p-value*)

It is widely acknowledged that the decline in aftershock activity over time (decay rate) is governed by the modified Omori law or Omori–Utsu law [49]. This law provides a description of the anticipated number of aftershocks occurring at a specific time after a mainshock event.

$$N(t) = \frac{K}{(c+t)^p} \quad (3)$$

where  $t$  shows the elapsed time since the mainshock. The constants  $K$ ,  $c$  and  $p$  collectively define the shape and characteristics of the aftershock sequence.  $K$ , which is related to the overall productivity of aftershocks, provides valuable insights into the shape and intensity of the sequence. It is dependent on the total number of earthquakes in the sequence. On the other hand,  $c$  represents the rate of activity in the initial phase of the sequence. It also signifies the characteristic time scale over which aftershock activity decays. Smaller values of  $c$  indicate a more rapid decay of activity. Lastly,  $p$  is associated with the power law decay of aftershocks and influences the rate at which aftershock activity declines over time. A higher value of  $p$  suggests a slower decay rate, while a lower value indicates a faster decay. By adjusting the parameters  $K$ ,  $c$ , and  $p$ , the particular seismic data can be tailored to suit a personalized model. Among these parameters,  $p$  holds the most significance and importance. Its range of variation is typically between 0.6 and 1.8, as observed in studies by [45,50]. It is worth noting that there may be variations of the Omori formula, and modifications can be made to account for different geological and seismological conditions. Furthermore, these parameters are often computed using statistical methods, such as Maximum Likelihood Estimation (MLE), based on observed seismic data.

The decay of aftershocks is believed to represent the rearrangement of stress caused by variations in stress resulting from the mainshock. The adjustment of stress can be seen as a reflection of the complex relaxation processes [51], as well as the structural heterogeneity within the source volume [49,52] associated with the geological framework of the area. It remains uncertain which physical factors hold significance in determining the  $p$ -value. The value of  $p$  seems to be unaffected by the magnitude of completeness,  $M_c$ . On the other hand, the  $c$ -value is largely influenced by  $M_c$  [53]. It is probable that the absence of data right after the initial earthquake is the reason why numerous minor aftershocks cannot be identified on seismograph readings. The knowledge surrounding the chaotic characteristics of the  $p$ -value in the crust is restricted. Various factors can be attributed to this phenomenon. For instance, [54] suggested that  $p < 1$  is commonly observed in aftershock series with normal mechanisms, whereas aftershocks that precede a large earthquake have  $p > 1$ . Significant attention is given to the determination of the  $p$ -value using the ML technique, as recommended by [55,56].

### 3.3. Spatial Aftershock Distribution (Correlation Integral and Fractal Dimension)

Fractal properties can be observed in fault networks and epicenter distributions [57,58]. Consequently, the seismic activity distribution can be examined by calculating the fractal dimension, also referred to as the  $D_c$ -value. This fractal dimension extends beyond Euclidean dimensions and quantifies the level of earthquake clustering. The application of fractal dimensions allows for the examination of self-similarity in fault tectonics and seismicity phenomena and processes.

Fractal distributions are unique in that they lack a specific length scale and are therefore suitable for describing scale-invariant phenomena. In a two-dimensional space, the decimal value of  $D_c$  can range from 0 to 2.0. When  $D_c$  values tend towards 0, the events are increasingly distributed on a singular point. As  $D_c$  approaches 1.0 in a space with 2-D, the event's distributions become more linear. This same trend can be observed in the events' distribution across a fracture. However, as  $D_c$  tends towards 2.0, the events become evenly distributed throughout the plane [59,60]. The correlation dimension is utilized to compute the  $D_c$  values, which are specified by [46] as follows:

$$D_c = \lim \left[ \frac{\log C(r)}{\log r} \right] \quad (4)$$

where the sphere radius being analyzed in the research is denoted as  $r$ , while the correlation integral is represented as  $C(r)$ :

$$C(r) = \frac{2N(R < r)}{N(N-1)} \quad (5)$$

The quantity  $N(R < r)$  represents the pairs count  $(X_i, X_j)$  that have a distance smaller than  $r$ . In the case of a fractal structure in the epicenter distribution, the subsequent correlation is derived:

$$C(r) \sim r^{D_c} \quad (6)$$

The fractal dimension, denoted as  $D_c$ , is specifically the correlation dimension [61]. The estimation of the fractal dimension of the spatial distribution of earthquakes is achieved through the utilization of this relationship. By plotting  $C(r)$  against  $r$  on a coordinate system with double logarithmic scales, the fractal dimension  $D_c$  can be determined. The fractal dimension ( $D_c$ ) value is derived by drawing a blue tangent line to the fractal curve typically at a log-log scale. This line represents the linear correlation between the logarithm of the number of boxes and the logarithm of the box size. The slope (gradient) of this tangent line indicates the fractal dimension. The distance  $r$  between two events,  $(\Theta_1, \Phi_1)$  and  $(\Theta_2, \Phi_2)$ , is measured by using a spherical triangle as described by Hirata [62]:

$$r = \cos^{-1} (\cos \theta \cos \theta_j + \sin \theta \sin \theta_j \cos(\phi_i - \phi_j)) \quad (7)$$

where  $(\theta_i, \varnothing_i)$  and  $(\theta_j, \varnothing_j)$  represent, respectively, the geographic coordinates (latitudes and longitudes) of the  $i$ th and  $j$ th events. A least-square line is fitted in the scaling region to obtain the slope.

### 3.4. Slip Ratio ( $S_P/S$ )

The slip, which refers to the relative displacement of points that were once adjacent on opposite sides of a fault, is a significant mechanism of crustal deformation. Typically, a portion of the slip takes place on the primary fault system, leading to the occurrence of the largest (and smallest) earthquakes, while the remaining slip occurs on the secondary fault segment [63]. The slip ratio, which represents the proportion of slip occurring on the primary fault compared to the total slip, can be determined by evaluating the spatial fractal dimension as:

$$\frac{S_P}{S} = 1 - 2^{-(3-D)} \quad (8)$$

where the slip at the principal fault ( $S_P$ ) and the cumulative slip along the fault system ( $S$ ), are two distinct measurements used to quantify the displacement along the fault [63,64]. When  $D_c$  equals 3, the complete slip rate is diverted towards the secondary faults, which are smaller in size. Conversely, when  $D_c$  is equal to 0, the entire slip is discharged on the principal fault.

The flowchart shown in Figure 4 illustrates the interconnections among the  $b$ -value,  $p$ -value, fractal dimension, and slip ratio. These relationships provide valuable insights into the seismicity, fault behavior, and earthquake hazard of the studied region. However, the precise nature of these relationships may differ based on the geological context and the specific characteristics of the seismic data under analysis.

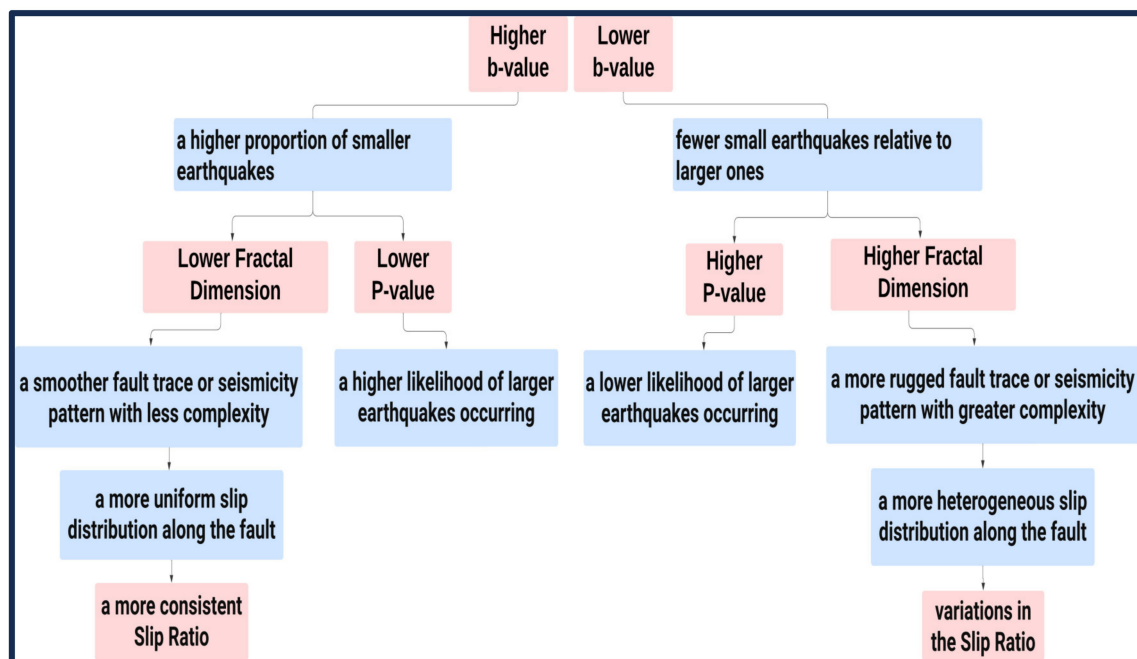


**Figure 4.** Flowchart representing the relationships between the  $b$ -value,  $p$ -value, fractal dimension, and slip ratio.

### 3.5. Coseismic Coulomb Stress Changes

Coulomb stress pertains to the shear stress exerted on a fault or rock mass due to tectonic forces. It quantifies the additional stress that can either facilitate or impede fault movement, depending on whether it aligns with or opposes the existing stress on the fault plane. In the fields of geology and seismology, Coulomb stress is utilized to evaluate the probability of earthquake occurrence and comprehend faulting mechanics. When the

Coulomb stress surpasses a specific threshold, it has the potential to initiate or hinder fault movement, potentially resulting in earthquakes or aseismic slip. This concept is crucial for comprehending fault behavior mechanics and assessing seismic hazards. In certain instances, an escalation in Coulomb stress may encourage fault slip, leading to larger coseismic displacements; while in other cases, it may impede fault slip, resulting in smaller displacements. Coseismic displacement denotes the movement or displacement that transpires along a fault during an earthquake, specifically during the earthquake's rupture period. It represents the instantaneous movement of rock masses on either side of a fault plane as a consequence of the accumulated strain being released during the seismic event. Alterations in Coulomb stress can influence the likelihood of fault slip and the magnitude of displacement during an earthquake. Moreover, the correlation between coseismic Coulomb stress and coseismic displacement can vary depending on factors such as the fault's geometry and orientation, the regional stress field, and the mechanical properties of the rocks surrounding the fault [65].

### 3.6. The Akaike Information Criterion (AIC): Description and Algorithm Validation

The Akaike Information Criterion (AIC) is derived from information theory and serves as a means to estimate the amount of information that would be sacrificed if a specific model were employed to describe the underlying process of the analyzed data [66]. By using AIC, one can compare and rank a collection of statistical models based on the extent of information loss in the investigated process. It is crucial to emphasize that AIC is solely applicable for comparative purposes and cannot determine the absolute quality of a model. The formula for AIC is expressed as follows:

$$AIC = n \cdot \ln(\sigma^2) + 2k \quad (9)$$

The variable  $n$  represents the quantity of data points,  $\sigma^2$  denotes the cumulative sum of squared residuals for the assessed model, and  $k$  signifies the count of independent parameters within the model. According to Equation (9), the optimal model is estimated by the minimum value of AIC that corresponds to the lowest  $\sigma^2$  value. Therefore, this model best represents the investigated process. For example, when comparing two potential models, their relative quality can be assessed by calculating the difference in AIC values. This approach can also be used in reverse, such as in the context of seeking a particular action within a time series. In such a scenario, two models are selected: one that precisely characterizes the desired conduct and another that represents a different behavior.

The forecast aftershock occurrences using Maximum Likelihood Estimation (MLE) and Root Mean Square (RMS) analysis involves several key parameters that are vital for understanding and forecasting seismic aftershock sequences. These parameters include Omori parameters ( $p$ -value,  $c$ -value, and  $k$ -value), and power-law decay parameters ( $pm$ ,  $cm$ , and  $km$ ), which control the initial level, decay rate, and time scale of aftershock activity, respectively. The parameter  $pm$  signifies the rate of aftershock occurrence immediately following the mainshock, with a higher value indicating a greater initial level of activity. Conversely,  $cm$  determines the speed at which aftershock rates decrease post-mainshock, where a higher  $cm$  value denotes a slower decay, indicating prolonged aftershock activity. The parameter  $km$  reflects the time frame over which aftershock rates decrease, with higher values suggesting a longer-lasting aftershock period. Additionally, statistical measures such as the Kolmogorov–Smirnov (KS) test, Hurst exponent ( $H$ ), KS statistic, and Root Mean Square (RMS) error are essential in assessing model fit and accuracy. The KS test evaluates how well predicted aftershock rates align with observed data, with a lower KS statistic indicating better agreement. The Hurst exponent quantifies long-term memory in aftershock occurrence patterns, with higher values indicating stronger persistence. The RMS error measures differences between predicted and observed values, with lower values signifying better predictive accuracy. Furthermore, parameters such as Effective Parameter Count ( $Epl$ ) and Best Model ( $Bst$ ) help assess model complexity and identify the most suitable model. Higher standard deviations ( $\sigma$ ) associated with  $Epl$  and  $Bst$  indicate greater

uncertainty in determining model complexity and selecting the best-fitting model, respectively. Overall, these parameters collectively contribute to a comprehensive understanding of aftershock behavior and aid in improving forecasting accuracy, while accounting for model uncertainty.

#### 4. Results and Discussions

A series of powerful aftershocks (reaching up to Mw 6.7) have been observed subsequent to the occurrence of two consecutive earthquakes measuring Mw 7.8 and 7.5 (on 6 February 2023) along the segments of the East Anatolian Fault Zone (EAFZ). The estimation of the earthquake distribution using the *b-value* and the decay rate of aftershocks (*p-value*) has been conducted using the magnitude–frequency relation of Gutenberg and Richter (Equation (1)) and the modified Omori law (Equation (3)), respectively. In order to obtain accurate *b-value*, events with a magnitude greater than the completeness magnitude ( $M_c$ ) were selected using the maximum curvature method.  $M_c$  holds significant importance in seismicity-based research as it allows for the analysis of a maximum count of events with high quality. For the entire sequence, the  $M_c$  of 4.4 was determined (Figure 5), resulting in a calculated *b-value* of  $1.21 \pm 0.03$ . The squares and triangles on the frequency–magnitude distribution plot often represent observed and estimated cumulative earthquakes for each magnitude value, respectively, which provide insights into the observed and predicted patterns of seismicity in the studied region (Figure 5). Xu et al. [67] conducted a study in the studied area to analyze the seismicity rates of events ranging from Mw 1–7 using the Gutenberg–Richter (G-R) law. Considering this, Melger et al. [68] explored two different scenarios. The first scenario involved investigating the seismicity rates since a major earthquake was historically reported in 1114 (Mw = 7.8) up until 2022, with *b-values* ranging approximately from 0.92 to 0.94. The second scenario focused on the period between 2007 and 2019, with *b-values* of 1.1. In our study, the *b-value* slightly surpasses those observed in the two scenarios mentioned and the global average of 1.0. This suggests that the Türkiye sequence is predominantly characterized by aftershocks with smaller magnitudes relative to larger ones, playing a role in regulating fluctuating crustal stress levels within the region, which reflects a more stable or less stressed seismic environment, where smaller earthquakes are more prevalent [45,46]. Figure 6 illustrates the rate at which aftershocks occurred within 80 days of the Türkiye earthquake doublet. The graph shows that the occurrence rate decreased rapidly from ~65 events per day immediately after the main shock, to ~15 events per day after the first 5 days, and then to about five events per day after 15 days. The rate then gradually declined over the course of 80 days. The decay characteristics of the Türkiye aftershock sequence were analyzed using the *p-value* of the modified Omori law, as shown in Figure 7. The parameters of Omori’s law primarily vary depending on the tectonic environment, such as the styles of faulting, in the region [11]. The observed *p-value* was found to be as low as  $1.1 \pm 0.04$ , which is slightly higher than the mean value of 1.0. A higher *p-value* indicates a faster decay of aftershock activity. The characteristic time scale, represented by the *c-value*, for the decay of aftershock activity was determined to be  $0.204 \pm 0.058$ . This suggests a relatively moderate or low initial productivity of aftershocks. The point at which the observed rate of aftershocks starts to follow the predicted decay pattern is known as the “decaying onset”. This point typically aligns closely with the parameter *c*, which helps adjust the model to match the start of the decay curve. By visually examining the graph representing the decay curve and identifying the *c* value (Figure 7), we can observe the moment when the curve starts to sharply decline from its peak. This adjusted point, determined by the *c* value, offers an estimate of when the decay rate begins to significantly decrease, indicating the onset of decay. The *c* parameter itself provides a quantitative estimate of this onset, representing the time offset from  $t = 0$  (the time of the mainshock) where the Omori–Utsu formula becomes a suitable fit for the data. Therefore, the value of *c*, expressed in the same time units as the *x*-axis of the graph (usually days), can be understood as the estimated day of the decaying onset following the mainshock. The constant (*k*-value) in the Omori formula, which is related to

the overall productivity of aftershocks, was calculated to be  $76.75 \pm 8.84$ . This suggests that the decrease in aftershock activity began between approximately 68 to 86 after the occurrence of the mainshocks, as shown in Figure 7. By comparing this outcome with Figure 6, we can infer that the decay in aftershock activity commenced 68 days following the mainshocks' occurrence.

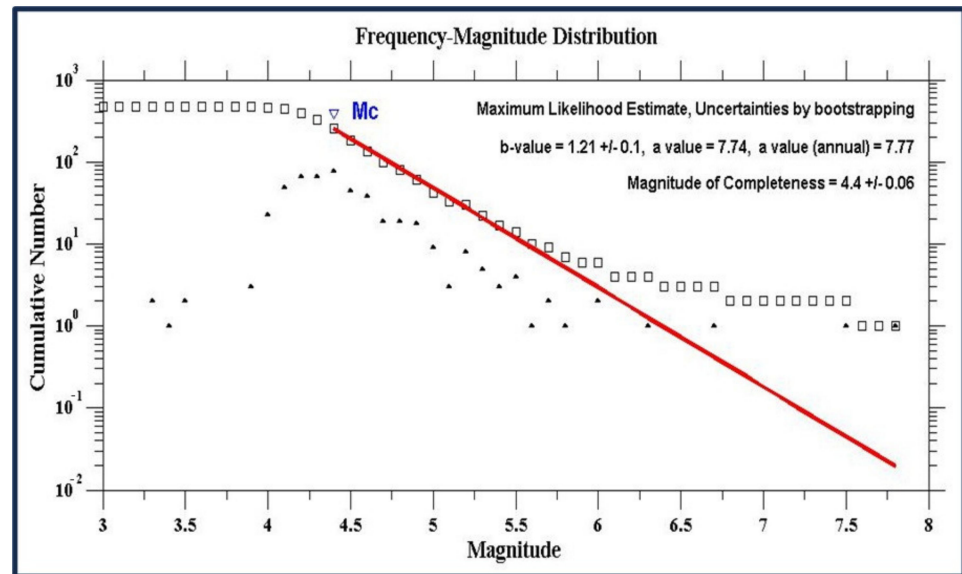


**Figure 5.** Frequency–magnitude distribution estimated by the maximum curvature technique for the period between 6 February 2023 and 10 January 2024.  $M_c$  is the cut-off magnitude. Squares and triangles show the observed and estimated cumulative earthquakes for each magnitude value, respectively.

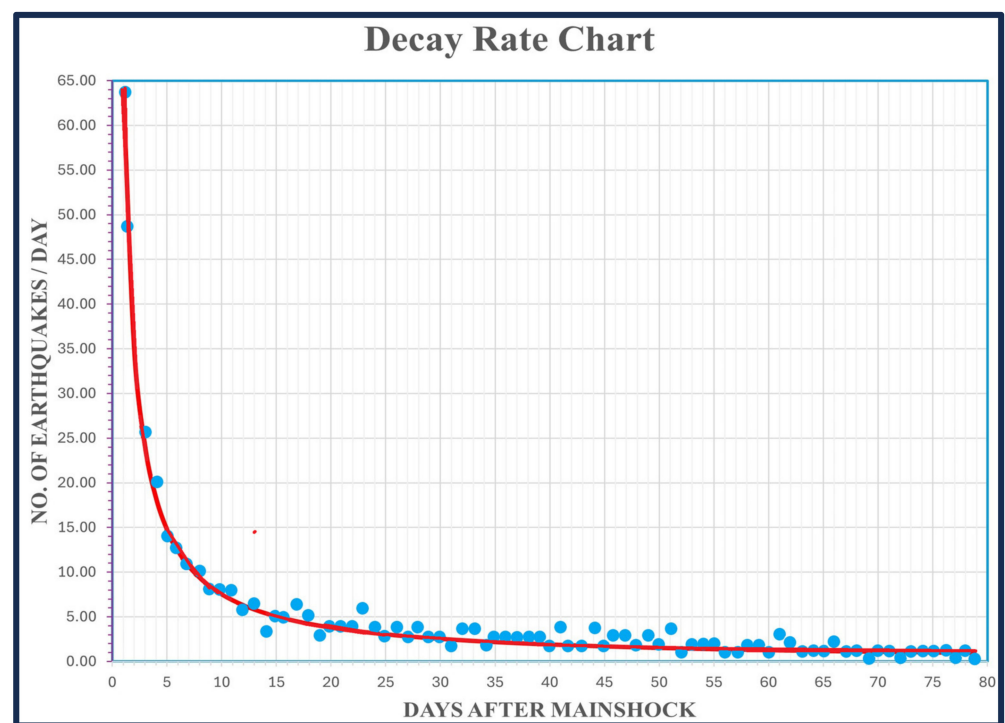


**Figure 6.** The decay rate at which aftershocks occurred within 80 days of the Türkiye earthquake doublet.

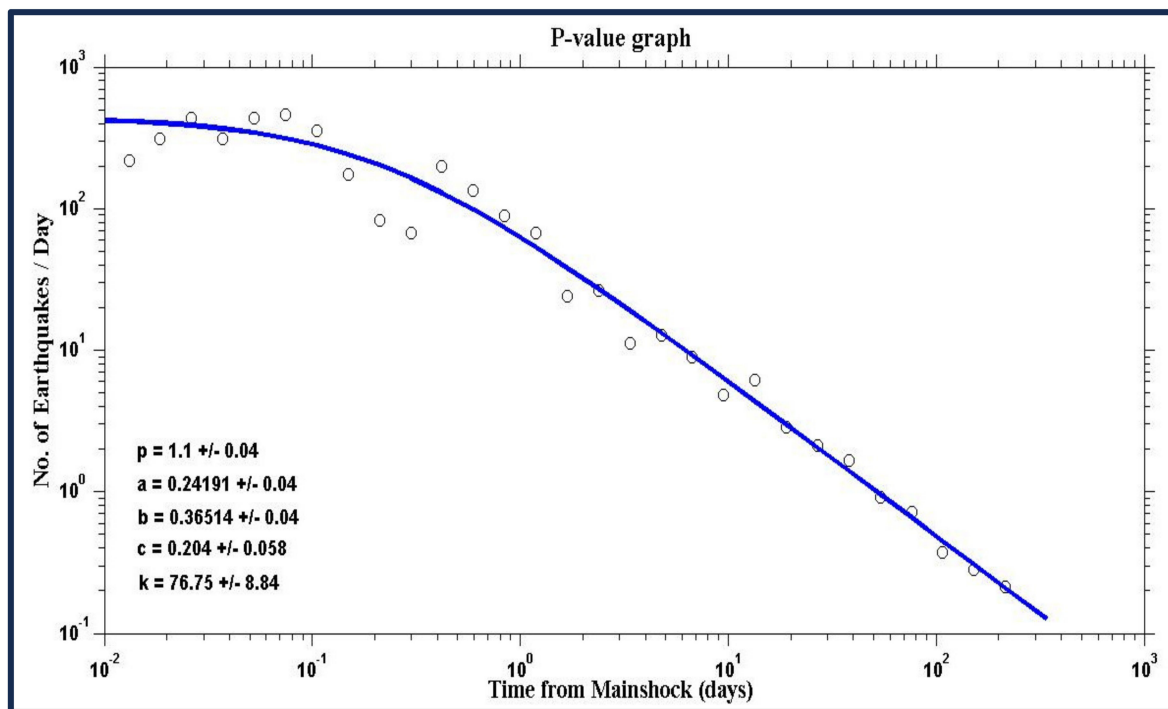


**Figure 7.** Decay rate of aftershock occurrence as a function of time following the mainshock for events with magnitude greater or equal to  $M_c$ , adjusted using the modified Omori law. The parameters of the relation  $p$ ,  $k$  and  $c$  and their standard deviations are given on the graph.

Bayrak and Kirci [69] conducted an analysis of active fault data along the East Anatolian Fault Zone (EAFZ) using both manual (classic) and modern versions of the box counting method. The fractal analysis revealed that the total fault length along the EAFZ is 450 km ( $15 \times 30$  km), with a fault area of 13,500 km<sup>2</sup>. The fractal dimensions of the main EAFZ fault trace, calculated using the manual box counting method, ranged from 0.81 to 1.47. The highest fractal dimension value (1.47) was observed in the Karliova region and its surroundings, while the lowest value (0.81) was found in the area around Hazar Lake. The fractal dimension values for the areas surrounding the two main shocks, were 1.15 and 1.21 (determined using the manual box counting method) and 1.01 and 1.13 (determined using the Free box and Grid methods), respectively. In contrast, Sarp [70] utilized the box-counting method to determine the fractal dimension of major fault networks along the EAFZ, resulting in values ranging from 0.90 to 1.23. In this study, the determination of the fractal dimension ( $D_c$ ) involved analyzing the characteristics of earthquake sites, including epicenters and hypocenters. To calculate the fractal dimension, the box-counting technique was utilized. The research area was partitioned into a series of smaller boxes, and the count of boxes with at least one earthquake was documented for different box dimensions. A linear relationship can be observed by graphing the quantity of boxes against the size of the box (both in a logarithmic scale). The data points corresponding to the chosen earthquakes on the fractal curve were determined, and logarithmic transformations were applied to them. The slope of the tangent line was then calculated using linear regression analysis. Following that, a blue tangent line was usually drawn on the fractal curve at a logarithmic scale. The slope of this line represents the fractal dimension. In the case of the Türkiye sequence, the fractal dimension (Figure 8) was determined to be  $0.99 \pm 0.03$  by analyzing the correlation integral and distance between hypocenters using data from 471 earthquakes. Despite considering the three-dimensional space, the fractal dimension value being smaller than 1.0 suggests that the events are clustered and distributed along the fault line. Xu et al. [67] indicated that the long-term slip rates inferred from GPS data prior to the latest significant earthquakes range from 3 to 7 mm/year. From the east to the west along the East Anatolian Fault (EAF), the slip rates substantially decrease to 1–4 mm/year.

The slip ratio that arises from the sequence of aftershocks pertains to the proportion of the overall fault slip that occurred during the seismic event, in relation to the total length of the fault rupture. This ratio quantifies the extent of fault slip relative to the length of the fault that was involved in the earthquake. In the case of the Türkiye sequence, where  $D_c = 0.99$ , the slip ratio is determined to be 0.75. In simpler terms, 75% of the total slip is attributed to the primary rupture during the Türkiye sequence, while the remaining 25% is distributed across the secondary rupture. Melgar et al. [68] demonstrated that the EAF exhibits a maximum slip of 8 m, primarily concentrated at depths ranging from 3 to 7 km, indicating a shallow slip deficit. Similarly, the Çardak fault experiences a maximum slip of 11 m during the Mw 7.6 aftershock, extending from the surface to a depth of 7 km.

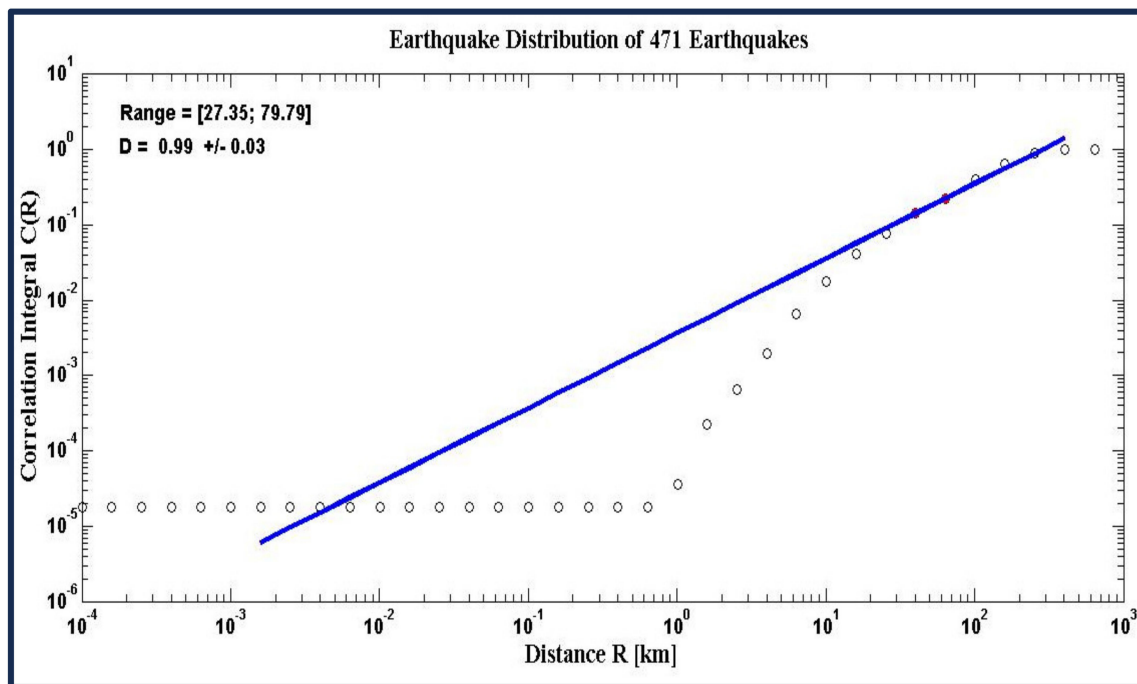


**Figure 8.** Fractal dimension ( $D_c$ ) of the seismic activity observed in the studied area.

The initial phase of the M 7.8 earthquake caused a rupture in a fault segment that spans approximately 50 km to the east of the main East Anatolian fault (EAF). This segment is located along the northern extension of the Dead Sea fault (DSF) in the southern region. The Coulomb stress changes resulting from this initial rupture indicate positive values to the northeast of the EAF, suggesting that this initial slip may have played a role in triggering slip on the EAF. The complete rupture of the Mw 7.8 earthquake, as observed through remote sensing, covered a section of the EAF that spans approximately 300 km. The resulting Coulomb stress changes on the Sürgü fault, which is an east-west trending fault in the area where the Mw 7.5 aftershock originated, also show positive values. This indicates that the M 7.8 event may have contributed to triggering the Mw 7.5 earthquake that occurred about 9 h later. Lastly, the Coulomb stress change modelling can be used to evaluate how the overall sequence of earthquakes, including the Mw 7.8 and Mw 7.5 events, has altered the regional stress state. Figure 9a illustrates the Coulomb stress change on left-lateral strike-slip faults that strike in a northward direction, similar to the DSF. The northern part of the DSF, just south of the Mw 7.8 epicenter, as well as the western end of the Sürgü fault, have been loaded. Figure 9b displays the Coulomb stress change on left-lateral strike-slip faults that strike in a northeastward direction, like the EAF. The majority of the EAF has been relieved of stress due to the mainshock slip on this structure, although there are still areas of stress increase at the ends of the rupture on the EAF [65].

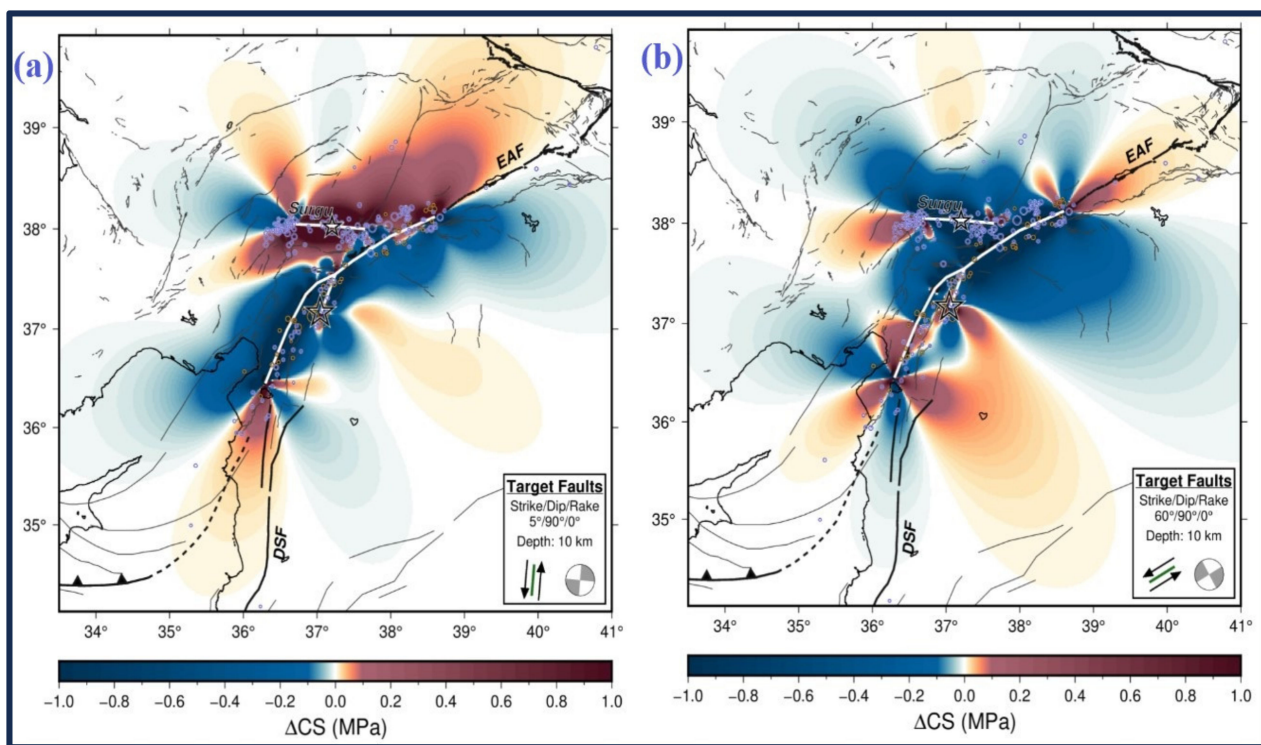


**Figure 9.** Coulomb stress (CS) alteration resulting from the full rupture detected via remote sensing for both the Mw 7.8 and Mw 7.5 Türkiye earthquakes combined. The stars represent the main shocks, white lines represent the segments of the fault used in the modelling, while the light purple circles are the seismicity. Key to fault names: Dead Sea fault (DSF), East Anatolian fault (EAF), and Sürgü fault. Red color indicates a fault has been brought closer to failing, and blue color indicates the fault is further from failing (Source: US Geological Survey, [52]).

The Akaike Information Criterion ( $AIC$ ) is a useful tool in aftershock modelling for comparing the fit of different models, such as the Maximum Likelihood Estimation (MLE) and the Root Mean Square (RMS) models, to observed aftershock data (Figure 10). Models with lower  $AIC$  values are better fitting, indicating that they provide a more accurate representation of the observed data. Aftershock modelling fit refers to how well a specific aftershock model, such as MLE or RMS, captures the observed patterns and behaviors of aftershocks following a mainshock. By comparing the predictions of these models to observed aftershock data, the  $AIC$  can be used as a quantitative measure to evaluate their fit. A lower  $AIC$  value suggests a better fit, indicating that the model provides a more accurate representation of the observed aftershock sequence. The Maximum Likelihood Estimation (MLE) is a statistical method utilized to estimate the parameters of a probability distribution that most accurately represents the observed data. In the context of aftershock activity, the MLE model is employed to estimate parameters such as the decay rate. On the other hand, the Root Mean Square (RMS) model is a physical model that describes the behavior of faults and the generation of earthquakes by considering frictional properties. The dashed vertical line at time = 20 days in Figure 10 represents the minimum  $AIC$  value or the  $AIC$  value of the best-performing model among those under comparison. Essentially, it signifies the model that offers the optimal trade-off between goodness of fit and complexity, as per the  $AIC$  criterion.

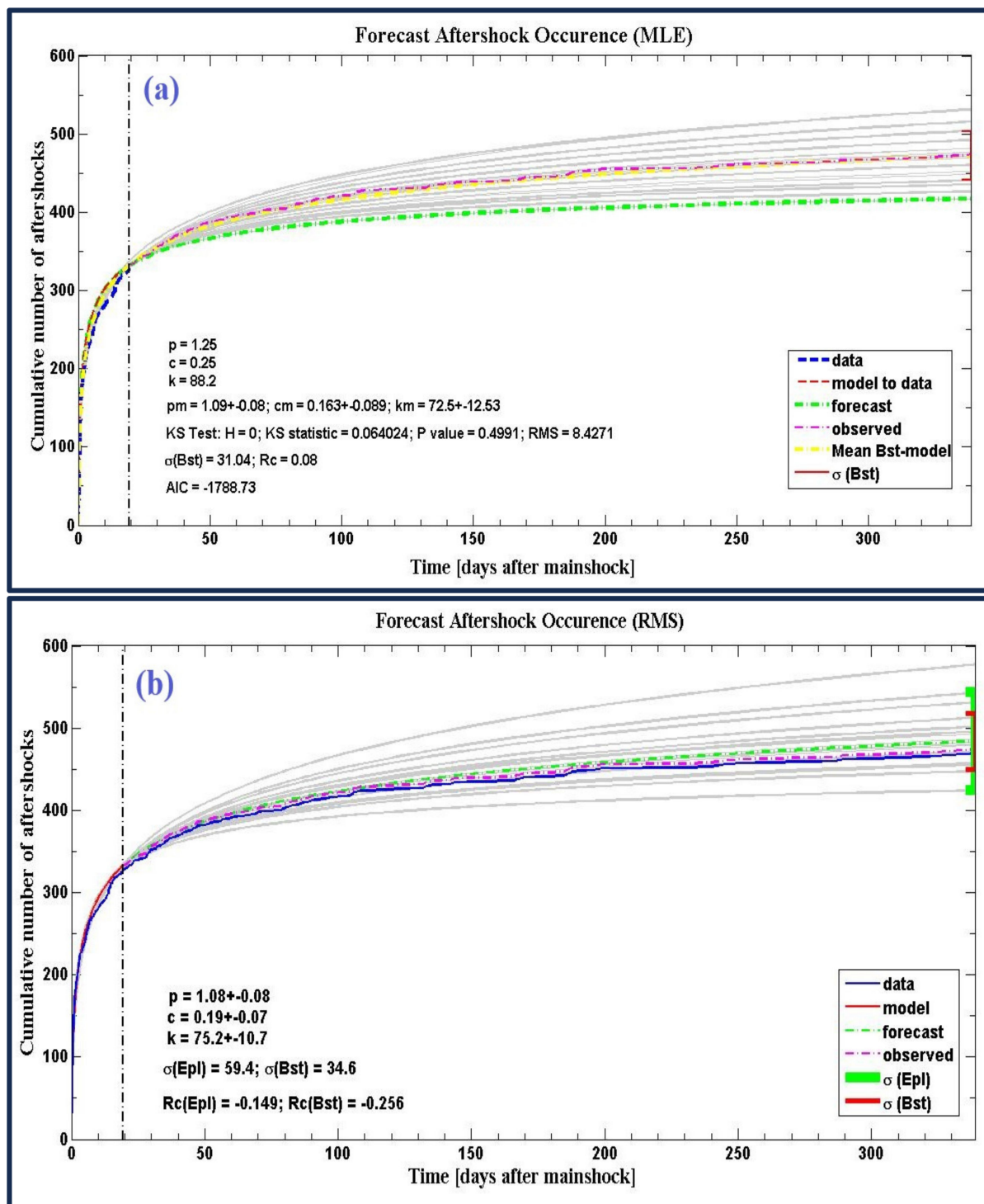


**Figure 10.** Forecast aftershock occurrences using (a) the Maximum Likelihood Estimation (MLE) model and (b) the Root Mean Square (RMS) model, to observed aftershock data following the Mw 7.8 and Mw 7.5 Türkiye earthquakes. The dashed vertical line typically represents a point of comparison between the models.

By utilizing the RMS model, it becomes possible to simulate the occurrence and behavior of aftershocks based on the fault's frictional characteristics. By analyzing the AIC, the optimal model that provides the best fit can be selected. In the case of forecasting aftershock occurrence using the MLE model, the following results are obtained: The Omori parameters indicate a decay rate of ( $p = 1.25$ ,  $c = 0.25$ , and  $k = 88.2$ ). Additionally, a

modified version of the Omori formula incorporates a power-law decay parameter, which shows values of ( $pm = 1.09$ ,  $cm = 0.163$ , and  $km = 72.5$ ). Furthermore, the Kolmogorov–Smirnov (KS) test is utilized to compare the observed data distribution with the expected distribution from the model, and supplementary statistics are also provided (Figure 11). The data presented include the null hypothesis ( $H = 0$ ), with a KS statistic of 0.064 and a  $p$ -value of 0.499. A higher  $p$ -value suggests that the model is a good fit for the data. The Root Mean Square ( $RMS = 8.427$ ) measures the average difference between observed and predicted values. Lower RMS values indicate a better fit. The standard deviation of the best-fit model,  $\sigma(Bst)$ , is 31.04. The seismicity rate change parameter,  $Rc$ , is 0.08. The AIC is used for model selection, where models with reduced AIC values suggest a more optimal trade-off between accuracy and complexity ( $AIC = -1788.73$ ). The forecasted aftershock occurrence using the RMS model yields the following results: The Omori parameters are ( $p = 1.08$ ,  $c = 0.19$ , and  $k = 75.2$ ). The standard deviations of the best-fit model for aftershock occurrence are  $\sigma(Epl) = 59.4$  and  $\sigma(Bst) = 34.6$ . A lower value indicates a better fit to the observed data. The parameters associated with seismicity rate changes are  $Rc(Epl) = -0.149$  and  $Rc(Bst) = -0.256$ . These parameters provide insights into the expected modifications in seismic activity, capturing the influence of the aftershock sequence on the overall seismicity rate. The evaluation of different models in representing the decline of aftershock rate over time has been evaluated, and the most optimal model is illustrated in Figure 11 and Table 1.

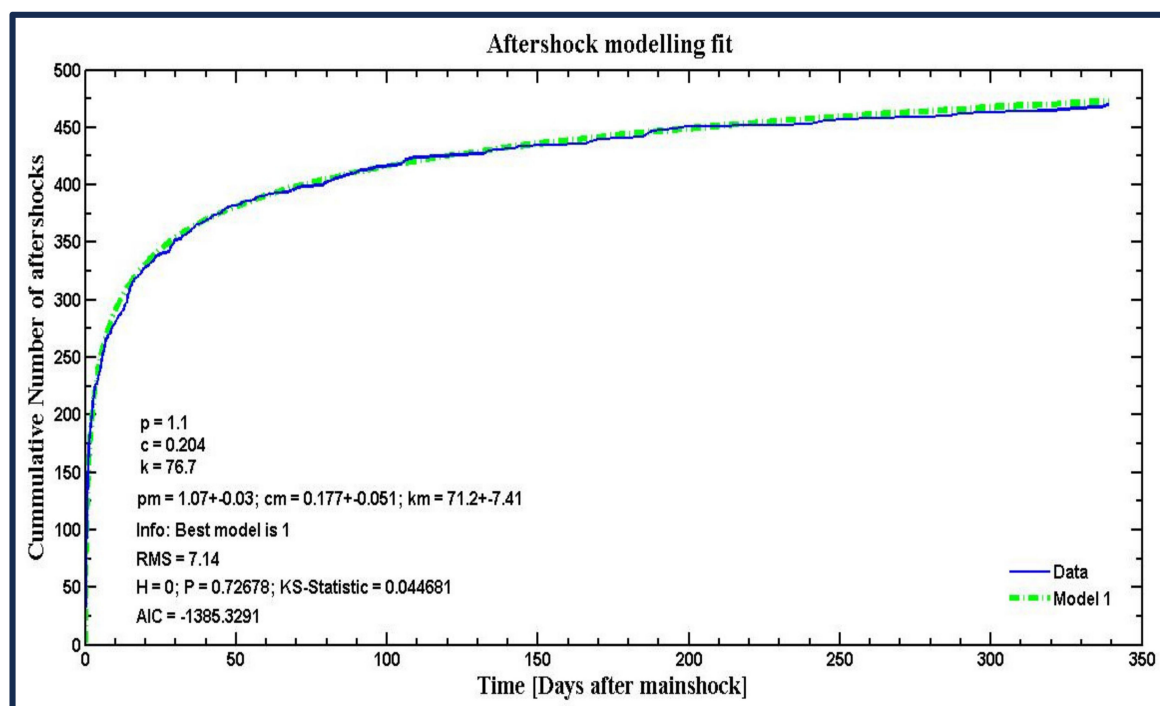


**Figure 11.** The aftershock modelling fit demonstrates the effectiveness of the optimal model in accurately representing the temporal decrease in aftershock rate over time.

**Table 1.** Comparison of decay parameters in forecasting aftershock occurrences using MLE, RMS, and Best-Fit models.

AIC Models	$p$ -value	$c$ -value	$k$ -value
MLE model	1.25	0.25	88.2
RMS model	1.08	0.19	75.2
Optimal model	1.1	0.204	76.7

## 5. Conclusions

The present study examines the occurrence of earthquakes during the Türkiye sequence through the use of statistical models and coseismic Coulomb stress modelling. To accomplish this objective, several parameters including *b-value*, *p-value*, *Dc-value*, slip ratio, and coulomb stress transfer were calculated. The estimated *b-value* is  $1.21 \pm 0.1$ , indicating that the East Anatolian Fault Zone (EAFZ) exhibits complex stress distribution patterns and frequent seismic activity characterized by larger magnitude aftershocks. This elevated *b-value* could be indicative of heterogeneity in the fault zone, potentially caused by the presence of fault asperities or variations in the crustal composition that impact stress accumulation and release mechanisms. The aftershock decay rate (*p-value* =  $1.1 \pm 0.04$ ) indicates that the frequency of aftershocks decreases linearly with time. In the context of the EAFZ, this implies a persistent release of stress post-mainshock, which is typical for fault zones with significant stored elastic energy and ongoing tectonic deformation. Meanwhile, the observed moderate *c-value* of  $0.204 \pm 0.058$  suggests a delay in the initiation of the aftershock sequence, possibly due to the complex rupture dynamics or the presence of barriers to rupture propagation within the fault zone. Additionally, the *k-value* of  $76.75 \pm 8.84$  indicates a substantial amount of aftershock activity, pointing to the release of a significant amount of accumulated stress over a relatively extended period following the mainshocks occurred, which nearly disappeared approximately 68 to 86 days after the occurrence of the main shocks. By referring to the decay rate chart we can infer that the decay in aftershock activity commenced 68 days following the mainshocks' occurrence. The fractal dimension *Dc*, determined using integral correlation, has been utilized to assess the slip ratio on the primary fault segment. The fractal dimension (*Dc*) of  $0.99 \pm 0.03$  suggests that aftershock activity is highly localized along the main fault trace or closely parallel subsidiary structures. This linear clustering is indicative of a distinct, dominant fault structure that significantly influences seismicity patterns. Analysis of the slip ratio during the aftershock activity reveals that 75% of the total slip occurred in the primary rupture, while the remaining portion was distributed across secondary faults, indicating that the aftershocks occurred on slightly fractured rock mass. This distribution could imply that a significant amount of strain along the fault was released during the mainshock, with the remaining 25% accommodated through aftershock activity and potentially aseismic slip. This high slip ratio could point to a highly dynamic rupture process during the mainshock, with significant implications for understanding the seismic hazard posed by future large events on the EAFZ. The earthquake sequence likely induced stress changes in the region's crust, potentially triggering or facilitating further rupture on neighboring faults. For instance, the Sürgü fault experienced the Mw 7.5 earthquake and significant aftershock activity. In sum, these parameters reveal a fault system characterized by complex stress distribution, significant heterogeneity, and a tendency to release accumulated tectonic stress through both seismic and aseismic mechanisms. The data suggest that the EAFZ is an active tectonic feature capable of generating large earthquakes and a complex aftershock sequence. This analysis can enhance seismic hazard assessment models for the region, particularly in predicting the distribution and magnitude of aftershocks following major seismic events. Moreover, understanding these dynamics can assist in preparing for future seismic activity through improved building codes, urban planning, and emergency response strategies.

In conclusion, this study has provided valuable insights into the underlying mechanisms of aftershock occurrences following recent major earthquakes in Türkiye. It has uncovered significant findings, including the rapid decrease in stress levels post-main shocks and the tendency towards clustering in aftershock seismicity. These findings challenge existing theories and contribute to a deeper understanding of earthquake dynamics. Our research has also addressed gaps in the current understanding of aftershock sequences in complex fault zones and demonstrated how it can be applied to improve predictive models for earthquake aftershock sequences globally. Additionally, by comparing our findings with existing literature, we have highlighted variations in aftershock characteristics, deepening our understanding of seismic activity variability and providing valuable

insights for future research endeavors. While this study focused on specific seismic events and models, the methodologies and insights gained can be extrapolated to assist in forecasting aftershock occurrences for future earthquakes. By refining our understanding of aftershock dynamics and enhancing the accuracy of forecasting models, we can establish a solid foundation for more effective strategies in assessing seismic hazards and managing disaster risks.

**Author Contributions:** S.M.A.: conceptualization, data curation, formal analysis, investigation, methodology. S.M.A. and K.A.: resources, validation, writing—review and editing. All authors have read and agreed to the published version of the manuscript.

**Funding:** This research has been funded by the Researchers Supporting Project Number (RSP2024R351), King Saud University, Riyadh, Saudi Arabia.

**Data Availability Statement:** The original contributions presented in the study are included in the article, further inquiries can be directed to the corresponding authors.

**Acknowledgments:** The authors express their gratitude to the Editor-in-Chief and the anonymous reviewers for their thorough evaluations, critical reviews, valuable feedback, helpful comments, and suggestions to improve this version of the manuscript. Deep thanks and gratitude to Researchers Supporting Project Number (RSP2024R351), King Saud University, Riyadh, Saudi Arabia for funding this article.

**Conflicts of Interest:** The authors declare no conflicts of interest.

**Disclaimer:** The views expressed herein are those of the authors and do not necessarily reflect the views of the CTBTO Preparatory Commission.

## References

1. Bozkurt, E.; Mittwede, S.K. Introduction to the geology of Turkey—A synthesis. *Int. Geol. Rev.* **2001**, *43*, 578–594. [\[CrossRef\]](#)
2. Barka, A. The 17 August 1999 Izmit Earthquake. *Science* **1999**, *285*, 1858–1859. [\[CrossRef\]](#)
3. Mendoza, C.; Hartzell, S.H. Aftershock patterns and main shock faulting. *Bull. Seismol. Soc. Am.* **1988**, *78*, 1438–1449.
4. King, G.C.P.; Stein, R.S.; Lin, J. Static stress changes and the triggering of earthquakes. *Bull. Seismol. Soc. Am.* **1994**, *84*, 935–953.
5. Thapa, D.R.; Tao, X.; Fan, F.; Tao, Z. Aftershock analysis of the 2015 Gorkha-Dolakha (Central Nepal) earthquake doublet. *Heliyon* **2018**, *4*, e00678. [\[CrossRef\]](#)
6. Ali, S.M.; Abdelrahman, K.; Al-Otaibi, N. Tectonic stress regime and stress patterns from the inversion of earthquake focal mechanisms in NW Himalaya and surrounding regions. *J. King Saud. Univ. Sci.* **2021**, *33*, 101351. [\[CrossRef\]](#)
7. Ali, S.M. Stress field and tectonic regime of the Eastern Mediterranean from inversion of earthquake focal mechanisms. *J. Asian Earth Sci.* **2024**, *262*, 106005. [\[CrossRef\]](#)
8. Rezapour, M. Aftershock Analyses of the Qotur Doublet-Earthquakes on 23 February 2020 in West-Azərbaycan Province, NW Iran. *Pure Appl. Geophys.* **2024**, *181*, 37–52. [\[CrossRef\]](#)
9. Zhang, Y.L.; Qi, H.N.; Li, C.Q.; Zhou, J. Enhancing safety, sustainability, and economics in mining through innovative pillar design: A state-of-the-art review. *J. Saf. Sustain.* **2023**, *in press*. [\[CrossRef\]](#)
10. Turkelli, N.; Sandvol, E.; Zor, E.; Gok, R.; Bekler, T.; Al-Lazki, A.; Karabulut, H.; Kuleli, S.; Eken, T.; Gurbuz, C.; et al. Seismogenic zones in eastern Turkey. *Geophys. Res. Lett.* **2003**. [\[CrossRef\]](#)
11. Tahir, M.; Grasso, J.R. Faulting style controls for the space–time aftershock patterns. *Bull. Seismol. Soc. Am.* **2015**, *105*, 2480–2497. [\[CrossRef\]](#)
12. Sayil, N. An application of the time- and magnitude-predictable model to long-term earthquake prediction in eastern Anatolia. *J. Seismol.* **2005**, *9*, 367–379. [\[CrossRef\]](#)
13. Gorüm, T.; Tanyas, H.; Karabacak, F.; Yılmaz, A.; Girgin, S.; Allstadt, K.E.; Süzen, K.L.; Burgi, P. Preliminary documentation of coseismic ground failure triggered by the February 6, 2023 Türkiye earthquake sequence. *Eng. Geology.* **1979**, *327*, 107315. [\[CrossRef\]](#)
14. Sengor, A.M.C. The North Anatolian transform fault: Its age, offset and tectonic significance. *J. Geol. Soc.* **1979**, *136*, 269–282. [\[CrossRef\]](#)
15. Ambraseys, N. *Earthquakes in the Mediterranean and Middle East: A Multidisciplinary Study of Seismicity Up to 1900*; Cambridge University Press: Cambridge, UK, 2009.
16. Taymaz, T.; Ganas, A.; Yolsal-Çevikbilen, S.; Vera, F.; Eken, T.; Erman, C.; Keleş, D.; Kapetanidis, V.; Valkaniotis, S.; Karasante, I.; et al. Source mechanism and rupture process of the 24 January 2020 Mw 6.7 Doganyol–Sivrice earthquake obtained from seismological waveform analysis and space geodetic observations on the East Anatolian Fault Zone (Turkey). *Tectonophysics* **2021**, *804*, 228745. [\[CrossRef\]](#)

17. Ali, S.M.; Akkoyunlu, M.F. Statistical analysis of earthquake catalogs for seismic hazard studies around the Karliova Triple Junction (eastern Turkey). *J. Afr. Earth Sci.* **2022**, *186*, 104436. [CrossRef]
18. Ambraseys, N.N. Temporary seismic quiescence: SE Turkey. *Geophys. J. Int.* **1989**, *96*, 311–331. [CrossRef]
19. Taymaz, T.; Eyidogan, H.; Jackson, J. Source parameters of large earthquakes in the East Anatolian Fault Zone (Turkey). *Geophys. J. Int.* **1991**, *106*, 537–550. [CrossRef]
20. Türkiye Earthquakes Recovery and Reconstruction Assessment. 2023. Available online: <https://www.sbb.gov.tr/wp-content/uploads/2023/03/Turkiye-Recovery-and-Reconstruction-Assessment.pdf> (accessed on 20 January 2024).
21. Over, S.; Demirci, A.; Ozden, S. Tectonic implications of the February 2023 Earthquakes (Mw7.7, 7.6 and 6.3) in south-eastern Türkiye. *Tectonophysics* **2023**, *866*, 230058. [CrossRef]
22. U.S. Geological Survey. M 7.5—Elbistan Earthquake, Kahramanmaraş Earthquake Sequence, USGS Earthquake Hazards Program. 2023. Available online: <https://earthquake.usgs.gov/earthquakes/eventpage/us6000jlqa> (accessed on 20 January 2024).
23. U.S. Geological Survey. M 7.8—Pazarcik Earthquake, Kahramanmaraş Earthquake Sequence, USGS Earthquake Hazards Program. 2023. Available online: <https://earthquake.usgs.gov/earthquakes/eventpage/us6000jllz> (accessed on 20 January 2024).
24. Reitman, N.G.; Briggs, R.W.; Barnhart, W.D.; Thompson Jobe, J.A.; DuRoss, C.B.; Hatem, A.E.; Gold, R.D.; Akçiz, S.; Koehler, R.D.; Mejstrik, J.D.; et al. *Fault Rupture Mapping of the 6 February 2023 Kahramanmaraş, Türkiye, Earthquake Sequence from Satellite Data: U.S. Geological Survey Data Release*; U.S. Geological Survey: Reston, VA, USA, 2023. [CrossRef]
25. Goldberg, D.E.; Taymaz, T.; Reitman, N.G.; Hatem, A.E.; Yolsal-Çevikbilen, S.; Barnhart, W.D.; Irmak, T.S.; Wald, D.J.; Öcalan, T.; Yeck, W.L.; et al. Rapid Characterization of the February 2023 Kahramanmaraş, Türkiye, Earthquake Sequence. *Seism. Rec.* **2023**, *3*, 156–167. [CrossRef]
26. Emre, Ö.; Duman, T.Y.; Özalp, S.; Elmacı, H.; Olgun, Ş.; Şaroğlu, F. *Açıklamalı Türkiye Diri Fay Haritası. Ölçek. 2013 1:1.250.000, Maden Tetkik ve Arama Genel Müdürlüğü, Özel Yayın Serisi-30, Ankara-Türkiye*; General Directorate of Mineral and Exploration Press: Ankara, Turkey, 2013; ISBN 978-605-5310-56-1.
27. Gutenberg, R.; Richter, C.F. Earthquake magnitude, intensity, energy, and acceleration. *Bull. Seismol. Soc. Am.* **1944**, *32*, 163–191. [CrossRef]
28. Utsu, T. A statistical study on the occurrence of aftershocks. *Geophysics* **1961**, *30*, 521–605.
29. Wiemer, S. A software package to analyze seismicity: ZMAP. *Seismol. Res. Lett.* **2001**, *72*, 373–382. Available online: <http://www.seismo.ethz.ch/en/research-and-teaching/products-software/software/ZMAP/> (accessed on 20 January 2024). [CrossRef]
30. Ishimoto, M.; Iida, K. Observations sur les séismes enregistrés, par le micro-seismographe construit dernièrement. *Bull. Earthq. Res. Inst. Univ.* **1939**, *17*, 443–478.
31. Mogi, K. Earthquakes and fractures. *Tectonophysics* **1967**, *5*, 35–55. [CrossRef]
32. Scholz, C.H. The Frequency-Magnitude Relation of Microfracturing in Rock and its Relation to Earthquakes. *Bull. Seismol. Soc. Am.* **1968**, *58*, 399–415. [CrossRef]
33. Wyss, M. Towards a physical understanding of the earthquake frequency distribution. *Geophys. J. R. Astron. Soc.* **1973**, *31*, 341–359. [CrossRef]
34. Papazachos, B.C. Foreshocks and earthquake prediction. *Tectonophysics* **1975**, *28*, 213–226. [CrossRef]
35. Allen, C.; Amand, P.; Richter, P.; Nordquist, J. Relation between seismicity and geological structure in the southern California region. *Bull. Seismol. Soc. Am.* **1965**, *55*, 752–797.
36. Utsu, T. Aftershocks and earthquake statistics (III): Analyses of the distribution of earthquakes in magnitude, time, and space with special consideration to clustering characteristics of earthquake occurrence. *J. Fac. Sci. Hokkaido University. Ser. 7 Geophys.* **1971**, *3*, 379–441.
37. Smith, W.D. The *b*-value as an earthquake precursor. *Nature* **1981**, *289*, 136–139. [CrossRef]
38. Imoto, M. Changes in the magnitude-frequency *b*-value prior to large ( $M > 6.0$ ) earthquakes in Japan. *Tectonophysics* **1991**, *193*, 311–325. [CrossRef]
39. Wiemer, S.; Mcnutt, S.; Wyss, M. Temporal and three-dimensional spatial analyses of the frequency-magnitude distribution near Long Valley Caldera, California. *J. Geophys. Res.* **1998**, *134*, 409–421. [CrossRef]
40. Jaume, S.; Sykes, L. Evolving towards a critical point: A review of accelerating seismic moment/energy release prior to large and great earthquakes. *Pure Appl. Geophys.* **1999**, *155*, 279–306. [CrossRef]
41. Ali, S.M.; Abdelrahman, K. Earthquake occurrences of the major tectonic terranes for the Arabian shield and their seismic hazard implications. *Front. Earth Sci.* **2022**, *10*, 851737. [CrossRef]
42. Ali, S.M.; Abdelrahman, K. The impact of fractal dimension, stress tensors, and earthquake probabilities on seismotectonic characterization in the red sea. *Fractal Fract.* **2023**, *7*, 658. [CrossRef]
43. El-Isa, Z.H.; Eaton, D.W. Spatiotemporal variations in the *b*-value of earthquake magnitude-frequency distributions: Classification and causes. *Tectonophysics* **2014**, *615–616*, 1–11. [CrossRef]
44. Mogi, K. Magnitude–frequency Relationship for Elastic Shocks Accompanying Fractures of Various Materials and Some Related Problems in Earthquakes. *Bull. Earthq. Res. Inst. Univ.* **1962**, *40*, 831–883.
45. Wiemer, S.; Katsumata, K. Spatial variability of seismicity parameters in aftershock zones. *J. Geophys. Res.* **1999**, *104*, 13135–13151. [CrossRef]
46. Wiemer, S.; Wyss, M. Mapping Spatial Variability of the Frequency-Magnitude Distribution of Earthquakes. *Adv. Geophys.* **2002**, *45*, 259–302.

47. Yadav, R.B.S. Seismotectonic Modelling of NW Himalaya: A Perspective on Future Seismic Hazard. Ph.D. Thesis, Department of Earthquake Engineering, IIT, Roorkee, India, 2009; 198p.
48. Aki, K. Maximum Likelihood Estimates of  $B$  in the Formula  $\log N = a - bM$  and its Confidence Limits. *Bull. Earthq. Res. Inst. Univ. Tokyo* **1965**, *43*, 237–239.
49. Utsu, T.; Ogata, Y.; Ritsuko, S.; Matsu'ura. The centenary of the Omori formula for a decay law of aftershock activity. *J. Phys. Earth* **1995**, *43*, 1–33. [[CrossRef](#)]
50. Olssen, R. An estimation of the maximum  $b$  values in the Gutenberg-Richter relation. *Geodynamics* **1999**, *27*, 547–552. [[CrossRef](#)]
51. Stein, R.S.; Wysession, M. *An Introduction to Seismology, Earthquakes and Earth Structure*; Blackwell Publishing: Oxford, UK, 2003; 498p, ISBN 0-86542-078-5.
52. Kisslinger, C.; Jones, L.M. Proprieties of Aftershocks in Southern California. *J. Geophys. Res.* **1991**, *103*, 424–453.
53. Utsu, T. Aftershocks and earthquake statistics (I)- Some Parameters which characterize an Aftershock Sequence and their Interaction. *J. Fac. Sci. Hokkaido University. Ser. 7 Geophys.* **1969**, *3*, 129–195.
54. Liu, Z.R. Earthquake frequency and prediction. *Bull. Seismol. Soc. Am.* **1984**, *74*, 255–265. [[CrossRef](#)]
55. Nyffenger, P.; Frolich, C. Recommendations for determining  $p$  values for aftershock sequence and catalogs. *Bull. Seismol. Soc. Am.* **1998**, *88*, 1144–1154. [[CrossRef](#)]
56. Nyffenger, P.; Frolich, C. Aftershock occurrence rate decay properties for intermediate and deep earthquake sequences. *Geoph. Res. Lett.* **2000**, *27*, 1215–1218. [[CrossRef](#)]
57. Turcotte, D.L. Fractals in geology and geophysics. *Pure Appl. Geophys.* **1989**, *131*, 171–196. [[CrossRef](#)]
58. Tiwari, R.K.; Paudyal, H. Gorkha earthquake (MW7.8) and aftershock sequence: A fractal approach. *Earthq. Sci.* **2022**, *35*, 193–204. [[CrossRef](#)]
59. Beauval, C.; Hainzl, S.; Scherbaum, F. The Impact of the spatial uniform distribution of seismicity on probabilistic seismic-hazard estimation. *Bull. Seismol. Soc. Am.* **2006**, *96*, 2465–2471. [[CrossRef](#)]
60. Spada, M.; Weimer, S.; Kissling, E. Quantifying a potential bias in probabilistic seismic hazard assessment: Seismotectonic zonation with fractal properties. *Bull. Seismol. Soc. Am.* **2010**, *101*, 2694–2711. [[CrossRef](#)]
61. Grassberger, P.; Procaccia, I. Measuring the strangeness of strange attractors. *Phys. D* **1983**, *9*, 189–208. [[CrossRef](#)]
62. Hirata, T. Fractal dimension of fault system in Japan: Fractal structure in rock fracture geometry at various scales. *Pure and Applied Geophysics*. In *Fractals in Geophysics*; Birkhäuser: Basel, Switzerland, 1989; pp. 157–170.
63. Khattri, K.N. Fractal description of seismicity of India and inferences regarding earthquake hazard. *Curr. Sci.* **1995**, *69*, 361–366.
64. Dimri, V.P. Fractals in geophysics and seismology: An introduction. In *Fractal Behaviour of the Earth System*; Dimri, V.P., Ed.; Springer: Berlin/Heidelberg, Germany, 2005; pp. 1–22. [[CrossRef](#)]
65. U.S. Geological Survey. Tectonic Map of Turkey Region. The 2023 Kahramanmaraş, Turkey, Earthquake Sequence, USGS Geologic Hazards Science Center and Collaborators. 2023. Available online: <https://earthquake.usgs.gov/storymap/index-turkey2023.html> (accessed on 30 January 2024).
66. Akaike, H. A new look at the statistical model identification. *IEEE Trans. Autom. Control* **1974**, *19*, 716–723. [[CrossRef](#)]
67. Xu, L.; Mohanna, S.; Meng, L.; Ji, C.; Ampuero, J.; Yunjun, Z.; Hasnain, M.; Chu, R.; Liang, C. The overall-subshear and multi-segment rupture of the 2023 Mw7.8 Kahramanmaraş, Turkey earthquake in millennia supercycle. *Commun. Earth Environ.* **2023**, *4*, 379. [[CrossRef](#)]
68. Melgar, D.; Taymaz, T.; Ganas, A.; Crowell, B.; Öcalan, T.; Kahraman, M.; Tsironi, V.; Yolsal-Çevikbilen, S.; Valkaniotis, S.; Irmak, T.S.; et al. Sub- and super-shear ruptures during the 2023 Mw 7.8 and Mw 7.6 earthquake doublet in SE Türkiye. *Seismica* **2023**, *2*, 3. [[CrossRef](#)]
69. Bayrak, E.A.; Kirci, P. Determination of the Fractal Dimension of the Active Fault Data along the East Anatolian Fault Zone. *Baltica* **2021**, *34*, 71–80. [[CrossRef](#)]
70. Sarp, G. Evolution of neotectonic activity of East Anatolian Fault System (EAFS) in Bingöl pull-apart basin, based on fractal dimension and morphometric indices. *J. Asian Earth Sci.* **2014**, *88*, 168–177. [[CrossRef](#)]

**Disclaimer/Publisher's Note:** The statements, opinions and data contained in all publications are solely those of the individual author(s) and contributor(s) and not of MDPI and/or the editor(s). MDPI and/or the editor(s) disclaim responsibility for any injury to people or property resulting from any ideas, methods, instructions or products referred to in the content.